Ultramicroscopy 113 (2012) 158–164

Contents lists available at SciVerse ScienceDirect

Ultramicroscopy

journal homepage: www.elsevier.com/locate/ultramic

Mapping defects in a carbon nanotube by momentum transfer dependent electron energy loss spectromicroscopy

Ebrahim Najafi [a,1], Adam P. Hitchcock [a,b,*], David Rossouw [c], Gianluigi A. Botton [b,c]

[a] Department of Chemistry, McMaster University, 1280 Main Street West, Hamilton, Ontario, Canada L8S 4M1
[b] Brockhouse Institute for Materials Research, McMaster University, Hamilton, Ontario, Canada L8S 4M1
[c] Department of Materials Science and Engineering, McMaster University, 1280 Main Street West, Hamilton, Ontario, Canada L8S4M1

ARTICLE INFO

Article history:
Received 4 July 2011
Received in revised form
16 October 2011
Accepted 23 November 2011
Available online 3 December 2011

Keywords:
Carbon nanotubes
Electron microscopy
Electron energy loss spectroscopy
q-dependence
Electron linear dichroism

ABSTRACT

Momentum resolved electron energy loss (EELS) spectra of multi-walled carbon nanotubes (MWCNT) have been measured at the C 1s edge in a transmission electron microscope (TEM). We demonstrate that structurally sensitive electron linear dichroic (ELD) signals analogous to X-ray linear dichroic (XLD) signals (Najafi et al., 2008) [17] can be measured by TEM-EELS from individual MWCNT if sample tilt and deflection of the inelastic scattering signal relative to the EELS spectrometer entrance aperture are used. This method is used to map defects in MWCNT at higher spatial resolution than is currently possible with X-ray microscopy.

1. Introduction

Multi-walled carbon nanotubes (MWCNT) are attractive reinforcing fillers for composite materials [1,2]. MWCNT-reinforced composites exhibit improved mechanical performance and electrical conductivity as well as resistance against thermal and radiation damage [3–5].

MWCNT are often functionalized through chemical reactions to overcome their limited solubility in common solvents, and to facilitate charge and load transfer between them and polymer matrices in composites [6–9]. However, chemical functionalization produces defects in MWCNT [10] which reduces their failure strain because defects serve as nucleation sites for fracture [11]. In addition, defects can impair the electrical and thermal conductivity of MWCNT [12,13].

In order to optimize MWCNT for targeted applications, it is necessary to quantify and map defects present. Conventional methods, such as Raman spectroscopy [14,15] and near edge X-ray absorption fine structure (NEXAFS) spectroscopy [16], sample large areas and therefore provide information relating only to the average property of an ensemble of MWCNT. Recently, we have used scanning transmission X-ray microscopy (STXM) to measure the X-ray linear dichroism (XLD) at the C 1s$\rightarrow\pi^*$ transition from individual MWCNT in order to evaluate their structural quality [17–19]. The XLD signal was found to be strong in high quality MWCNT and weak in defective ones. Thus, maps of the XLD signal along individual MWCNT act as maps of sp^2 defect density [18] (we define sp^2 defects as deviations from a perfect graphitic-like sp^2 structure). Furthermore, the C 1s$\rightarrow\pi^*$ XLD signal of bundles of high quality single-walled carbon nanotubes (SWCNT) was found to be similar to that observed in high quality MWCNT [19].

Although STXM can map sp^2 defects, thus providing a method of evaluating defect distributions in individual MWCNT, STXM has limited spatial resolution (typically ~25 nm; 10 nm is the record so far achieved [20]). Here, we explore the use of momentum transfer (q)-dependent electron energy loss spectroscopy (EELS) measured in a transmission electron microscope (TEM) to obtain electron linear dichroic (ELD) information similar to XLD measured in STXM, but at a much higher spatial resolution. In order to demonstrate the sensitivity of the measured dichroic signals to structural quality of CNT, we report an example of using ELD signals measured by q-dependent TEM-EELS to map defects in a MWCNT.

Linear dichroic signatures have been measured with a dedicated scanning transmission electron microscope (STEM) or TEM-EELS using a number of different techniques [21–26]. However, to the best of our knowledge, q-dependent EELS spectroscopy and imaging using the method described in this work, which provides information close to that provided by the STXM dichroism

* Corresponding author at: Brockhouse Institute for Materials Research, McMaster University, Hamilton, ON, Canada L8S 4M1.
Tel.: +1 905 525 9140x24749; fax: +1 905 521 2773.
E-mail address: aph@mcmaster.ca (A.P. Hitchcock).
[1] Present address: Department of Chemical Physics, California Institute of Technology, Pasadena, CA 91125, USA.

0304-3991/$ - see front matter © 2011 Elsevier B.V. All rights reserved.
doi:10.1016/j.ultramic.2011.11.017

measurements, has not been reported previously for carbon nanotubes, although it has been applied to the Ti 2p EELS spectrum of the rutile form of TiO_2 [27]. The first q-dependent TEM-EELS study of CNT was a comparison of C 1s EELS spectra of the edge and center of a MWCNT which showed a small change in the relative intensities of the C $1s \rightarrow \pi^*$ and C $1s \rightarrow \sigma^*$ transitions when the spectra were normalized in the continuum [21]. The spectral changes were interpreted as being due to changes in the orientation of graphitic-like planes relative to a fixed distribution of q directions. The observation of this type of edge/center effect has been repeated and its interpretation extended by Sun and Yuan [22] who have also defined experimental conditions to measure dichroic-free (so-called 'magic angle') TEM-EELS of high aspect ratio structures [23]. However the edge/center comparison is not the same as the anisotropic core excitation signal measured in the STXM studies. In the latter, NEXAFS spectra measured with the electric vector (E) either perpendicular or parallel to the long axis of MWCNTs are compared. However in the edge/center TEM-EELS studies reported to date, the measured signals are integrated over a range of q orientations, although the average q favors direction perpendicular with respect to the beam direction.

The spatial orientation of q relative to a sample can be manipulated in several different ways in a modern TEM. Part of this study consisted of exploring those different ways to find the way to measure the ELD signal directly analogous to the XLD signal measured in STXM. For brevity only the method finally used to measure that signal is described in this paper. Alternative methods and the path followed to choosing this method are outlined in Appendix A.

2. Experimental method

2.1. Sample preparation

MWCNT produced by an arc discharge (AD) method were purchased from MER Corporation (MERCorp) and used as-received. To prepare samples for TEM-EELS studies, MWCNT were dispersed in N,N-dimethylformamide (DMF) under bath sonication. The samples were sonicated for less than two minutes to minimize modification of their chemical, physical, and electronic properties [28]. The solutions were drop cast onto holey carbon grids (SPI Inc.); the grids were left to dry overnight and then further dried in a vacuum oven for 7 days at 200 °C.

2.2. TEM-EELS measurements

TEM-EELS data was measured using a FEI Titan 80–300 Cubed microscope (identified hereafter as Titan 1) in STEM mode. Titan 1 was operated at 80 kV using a high brightness field emission gun to minimize knock-on damage of MWCNT. Titan 1 is equipped with a Wien-type monochromator to reduce chromatic aberration of the electron beam and to improve the energy resolution of energy loss spectra. The microscope is located in an ultra-stable environment to allow stable operation over a period of several days without realignments of the microscope. The spectra were recorded in parallel detection mode using a post-column Gatan Tridiem 866 high resolution imaging filter. The energy resolution was better than 0.15 eV as measured at the zero-loss peak. The dwell time for spectral acquisition at each pixel was 0.5 s for on-axis measurements and 16 s for off-axis measurements. The convergence angle of the incident beam and collection angle of the scattered beam for the measurements are presented in Table 1. The choice of convergence angle is a compromise between optimizing momentum resolution and experimental counts. Reducing the condenser aperture size increases the momentum resolution. However, use of a very small condenser aperture would require prohibitively long acquisition times for adequate S/N in recorded spectra. The same is true of changing the size of the EELS collection aperture. It is also important to consider the collection angle formed by the EELS entrance aperture. To optimize recorded spectral counts, the camera length (magnification in diffraction mode) was chosen such that the central disk in the convergent beam electron diffraction (CBED) pattern, which is limited by the condenser aperture, is approximately the same size as the EELS entrance aperture. This establishes a situation where the convergence angle is the same as the acceptance angle. Although, in principle smaller convergence and collection angles could have given even better momentum resolution, experimentally we were able to demonstrate that these conditions gave us sufficient momentum resolution to clearly see the anisotropy; so much so that the π component was almost entirely suppressed when probing the long direction of the tubes.

Table 1
Experimental conditions used for TEM-EELS measurements.

	Energy (kV)	α (mrad)	β (mrad)
Figs. 3, 4, 6, 7	80	8.4	6.6
Figs. 1, A-3, A-4	80	6.5	4.5

3. Results

3.1. Principles of the method

In EELS, the electron scattering vector (q) is defined as the difference between the wave vector of the incident (k_0) and scattered (k_1) electrons (Fig. 1a) [29]. The differential cross section for inelastic electron scattering [29] indicates that the intensity of an electric dipole transition induced by inelastic scattering is related to the angle (γ) between q and the transition moment vector (r, which encodes

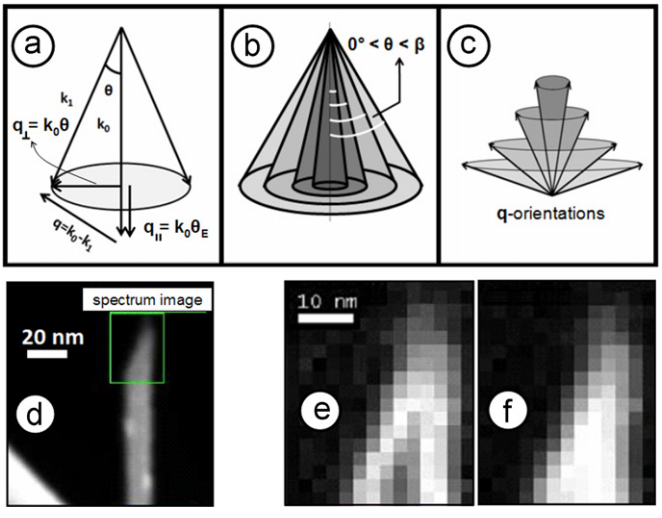

Fig. 1. (a) Definition of momentum transfer in EELS, and its relationship with the wave vectors k_0 and k_1; the gray surface represents all possible values for k_1 for a given energy loss. (b) Scattering angle of the collected electrons which varies between 0° and β. (c) Possible q orientations for the collected electrons for different energy losses ($q_{\parallel}$ has fixed length for a given energy loss). (d) MWCNT selected for measurement of the C 1s spectra of the edge and center (see Fig. A-2) in the tip region. (e) π^* image obtained by subtracting the averaged image of the pre-edge region (270–275 eV) from the averaged image of the π^* region (283–288 eV). (f) σ^* image obtained by subtracting the averaged image of the pre-edge region (270–275 eV) from the averaged image of the σ^* region (288–293 eV).

the directionality of the unoccupied state) according to

$$I \propto \cos^2 \gamma \quad (1)$$

In principle, this relationship allows the use of q-dependent TEM-EELS to study the structural anisotropy of materials.

The conventional approach to control and manipulate the orientation of q in TEM-EELS involves operating the microscope in diffraction mode and changing the collection angle (β) by changing the size of the spectrometer entrance aperture and/or the camera length. The scattering angle (θ) of the collected electrons varies between 0° and β (Fig. 1b) which produces a complex set of q orientations (Fig. 1c). Leapman et al. [30] showed that when a large aperture is used (large β), a wide range of scattered electrons are collected. These electrons carry an average q with a direction predominantly perpendicular to the beam ($q_\perp$) (Appendix Fig. A-1a). As the size of the aperture decreases, the range of the angular acceptance of the scattered electrons decreases which enhances the component parallel to the beam ($q_\parallel$) (Fig. A-1b). This method was further extended by Botton et al. [24] who generated 2D momentum-dependent energy-filtered diffraction patterns. Leapman et al. [30] used this approach to study the electronic properties of graphite and boron nitride films. Specifically, they used a small collection aperture to enhance $q_\parallel$ and then tilted the films to study intensity variations as a function of tilt angle. By tilting the sample up to 45° relative to the electron beam they could sample a full range of scattering angles including parallel and perpendicular to the electron beam. Stéphan et al. [21] used a closely related approach to study the structural anisotropy in MWCNT where they employed a large entrance aperture (and a large convergence angle) to enhance $q_\perp$. They used this geometry to investigate spectral differences between the edge and the center of a MWCNT. Browning et al. [31] proposed an alternative approach which is based on comparison of the energy loss spectra recorded at both small and large collection angles. Sun and Yuan [22] used this approach to record C 1s spectra from the edge and center of a MWCNT. At small collection angle, they observed that the C 1s→π^* transition was weak at the edge but strong at the center of a MWCNT. At large collection angle, the trend reversed and the C 1s→π^* transition became strong at the edge and weak at the center.

An example of such anisotropic differences in MWCNT is illustrated in Fig. 1. Fig. 1d presents an image of the tip of an AD-MWCNT, extending into vacuum from a lacey carbon support. A spectrum image measurement was made over the highlighted region at the tip of the MWCNT with the EELS conditions such that the average q was perpendicular to the beam (experimental conditions provided in Table 1). Fig. 1e is the π^* image obtained by subtracting the averaged image of the π^* region (283–288 eV) from the averaged image in the pre-edge region (270–275 eV). Fig. 1f is the σ^* image obtained by subtracting the averaged image of the σ^* region (288–293 eV) from the averaged image of the pre-edge region (270–275 eV). These EELS images clearly show that the C 1s→π^* transition is strong at the edge and weak at the center. In contrast the C 1s→σ^* transition has a more uniform intensity throughout the region sampled.

In this work we have overcome the limitations of the spatially resolved measurements in STEM with large incident and collection angles by measuring the spectrum with the inelastically scattered electron distribution laterally displaced relative to the EELS acceptance aperture. In this way, it is possible to more accurately control the direction of q relative to the sample and maintain high momentum resolution. Fig. 2 outlines the principle of this approach which is based on that of Botton [25], Saitoh et al. [26], and Radtke et al. [32]. By displacing the inelastically scattered electron distribution relative to the EELS entrance aperture and tilting the sample it is possible to collect EELS signal

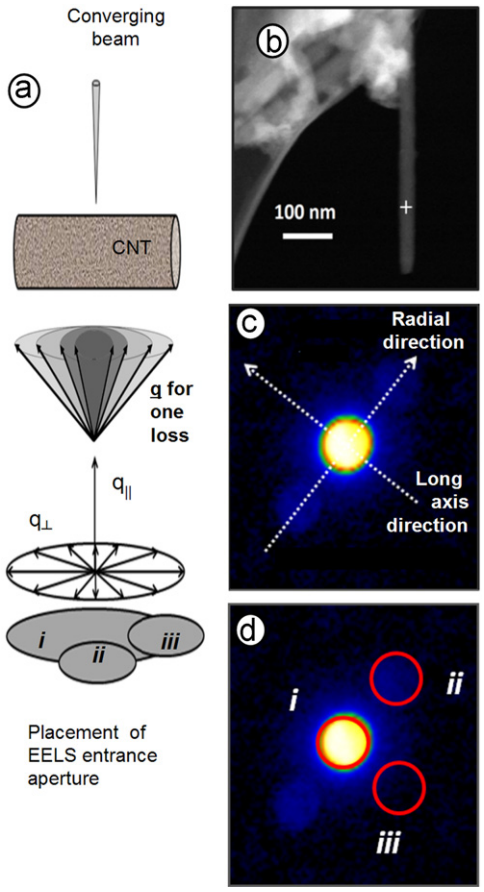

Fig. 2. (a) Sketch of how an off-axis EELS collection aperture can be used to control q directionality. For condition (i) the EELS spectrometer collects all orientations of $q_\perp$; for ii) it collects $q_\perp$ with perpendicular orientations relative to the long axis of the MWCNT; and for iii) it collects $q_\perp$ with parallel orientations relative to the long axis of the MWCNT. (b) Dark field STEM image of a high quality MWCNT used to demonstrate the procedure. (c) Convergent beam diffraction pattern (from the white cross in (b); the arrows show the radial and long axis directions of the tube. (d) Annotation of the convergent beam diffraction pattern to indicate how displacement of the scattering pattern relative to the EELS entrance aperture can be used to sample conditions (i), (ii), and (iii).

where $q_\perp$ dominates and the q vector has a specific orientation relative to an anisotropic sample such as a MWCNT.

The MWCNT studied is shown in Fig. 2b. A convergent beam diffraction pattern (Fig. 2c) was acquired from the MWCNT at the position marked with a cross in Fig. 2b using a 6.5 mrad convergence semi-angle of the incident probe (α=6.5 mrad) and a 4.5 mrad collection semi-angle (β=4.5 mrad), defined by the size of the EELS collection aperture. Fig. 2c labels the electron scattering signal associated with the short axis (radial direction) and the long axis of the MWCNT. Fig. 2d outlines the strategy to obtain two well defined orientations of $q_\perp$ relative to the MWCNT. At 80 kV incident electron energy, the characteristic angle (θ_E) at 285 eV is 1.8 mrad. At position *i* (beam centered on the EELS entrance aperture) with the collection angle of 4.5 mrad, the majority of scattered electrons are collected. Therefore, anisotropic information is lost in this geometry. However, when the inelastically scattered electron distribution is deflected such that the collection aperture is at position *ii*, the scattered electrons which enter the spectrometer correspond to $q_\perp$ with orientation perpendicular to the long axis of the MWCNT. When the inelastically scattered electron distribution is deflected such that the collection aperture is placed at position *iii*, the scattered electrons which enter the spectrometer correspond to $q_\perp$ with orientations parallel to the long axis of the MWCNT.

3.2. q-dependent TEM-EELS of a high quality AD-MWCNT

Arc discharge MWCNT are predominantly straight with highly ordered graphitic walls. Fig. 3a is a low resolution TEM image of the MWCNT selected for angle-dependent TEM-EELS studies (it is the same CNT as shown in Fig. 2b). Various forms of impurity by-products are found, such as those within the dotted circle. High resolution TEM (HRTEM) imaging reveals these impurities to be mostly graphitic structures. The HRTEM image of the MWCNT recorded for rectangle *b* in Fig. 3a is shown in Fig. 3b. While the inner layers in the MWCNT are highly ordered, the outer layers are somewhat distorted. This is due to surface oxidation which transforms sp^2 bonds into sp^3 bonds and peels off the layers [33]. The central hollow of the MWCNT has a diameter of ~2.6 nm and remains uniform along the tube.

A series of electron energy loss spectra of this MWCNT were measured along the line indicated in Fig. 3b. Fig. 4a shows the spectra of the edge (green) and center (red) of the MWCNT recorded when the entrance aperture is accepting the scattering signal such that the *q*-vector is parallel to the long axis of the tube (see inset to Fig. 4a). The definition of center and edge in MWCNT is given in Fig. A-2. The spectra are very similar and both show weak C 1s→π^* transitions. This contrasts strongly with the large differences seen in the π^* intensity for edge/center spectra reported by Stéphan et al. [21] and Sun and Yuan [22] but it is consistent with a well defined localization of the direction of *q* along the long axis of the tube, for which the C 1s→π^* transition is forbidden [17–19]. Fig. 4b shows the spectra of the edge and center of the MWCNT recorded when the entrance aperture is accepting the scattering signal such that the *q*-vector is perpendicular to the long axis of the tube (see inset to Fig. 4b). In this scattering geometry there is now a large difference between these two spectra with a strong C 1s→π^* transition in the spectrum at the edge but a weak one in the spectrum at the center of the MWCNT. This is consistent with a well defined localization of the direction of *q* across the tube, for which the C 1s→π^* transition is allowed at the edge but forbidden at the center [17–19]. Note that this scattering geometry gives the same result as reported by Stéphan et al. [21] and Sun and Yuan [22] but with enhanced differentiation of the two *q*-directions.

To further demonstrate the directionality of *q*, and to produce *q*-direction dependent ELD signals directly analogous to XLD measurements with STXM-based photoabsorption [17–19], the dependence of the C 1s spectrum of the MWCNT was investigated as a function of the MWCNT tilt (Fig. 5a). By using a high-tilt tomography holder, the MWCNT was oriented at 77° relative to horizontal in a plane perpendicular to the beam. The entrance aperture was placed to collect $q_\perp$ parallel to the MWCNT (similar to the geometry shown in inset of Fig. 4a). Then, angle-dependent spectra from the center of the same MWCNT were recorded at several tilt angles. Specifically, the spectra were extracted from the center of linescans recorded across the MWCNT. At zero tilt,

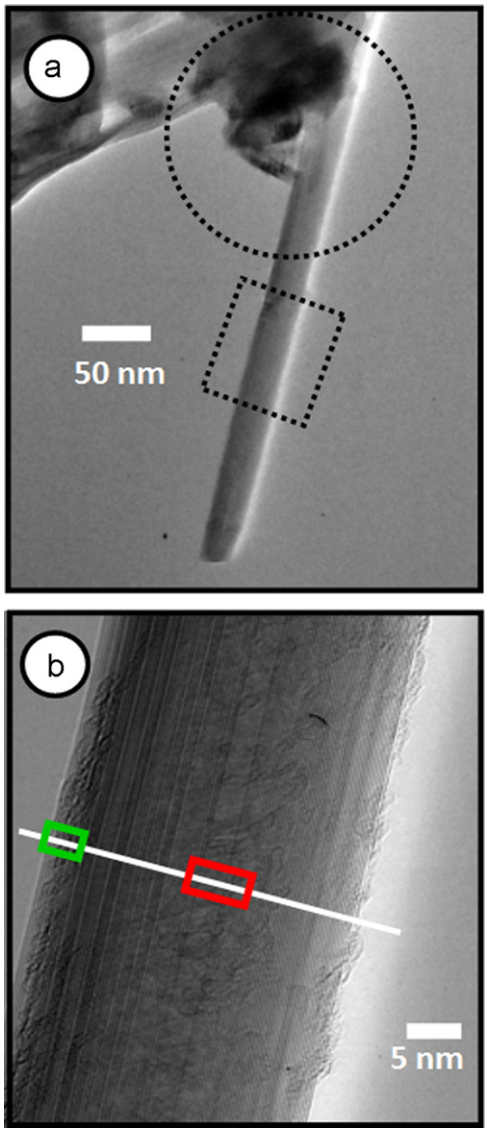

Fig. 3. (a) Low resolution TEM image of the MWCNT studied (diameter ~35 nm; length ~1.5 μm). (b) High resolution (HRTEM) image of the MWCNT recorded from rectangle b in (a). The line indicates the trajectory of the linescan spectral measurement while the green (left) and red (right) boxes indicate the edge and centre areas sampled. (For interpretation of the references to color in this figure legend, the reader is referred to the web version of this article.)

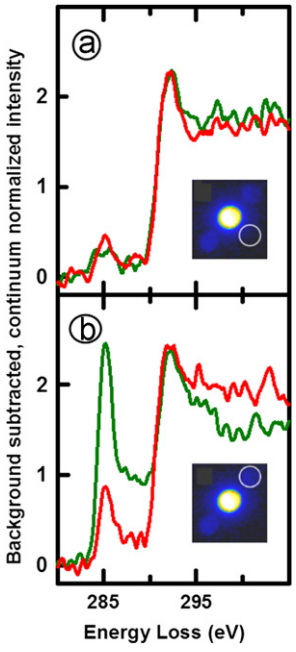

Fig. 4. (a) C 1s spectra of the edge (green) and centre (red) of the MWCNT in Fig. 3b extracted from linescan spectra recorded with $q_\perp$ parallel to the long axis of the MWCNT. (b) C 1s spectra of the edge (green) and centre (red) from linescan spectra recorded with $q_\perp$ perpendicular to the long axis of the MWCNT. The displacement of the inelastic scattering relative to the aperture is indicated in the inset figures. For each spectrum, a background extrapolated from the pre-C1s signal has been subtracted, and the intensity has been scaled to set the intensity at 350 eV to 1. (For interpretation of the references to color in this figure legend, the reader is referred to the web version of this article.)

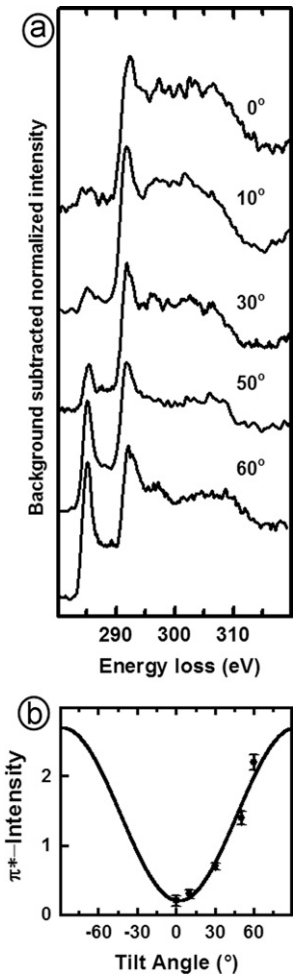

Fig. 5. (a) C 1s EELS spectra of the centre of the MWCNT in Fig. 3b extracted from linescans recorded at the indicated sample tilt angles. The linescans were recorded with $q_\perp$ parallel to the long axis of the MWCNT. (b) π^* intensities at the centre of the MWCNT (circles, with error bars) plotted versus tilt angle, fit to the polarization function (Eq. (2)) (solid line).

the intensity of the C1s$\rightarrow\pi^*$ transition is very weak since it is forbidden (Fig. 5a). When the MWCNT is systematically tilted to higher angles (up to 60°), the intensity of the C1s$\rightarrow\pi^*$ transition progressively increases. After subtracting a background extrapolated from the pre-C1s signal and unit normalization of the C 1s continuum intensity at 350 eV (which is needed as the beam passes through different amounts of sample as the tilt angle changes), the C 1s$\rightarrow\pi^*$ intensity was integrated. This π^* intensity is plotted as a function of tilt angle in Fig. 5b. If the angle dependence of the intensity corresponds to linear dichroism, the intensities should depend on tilt angle according to

$$I_{\pi^*}(\theta) = A + B\cos^2(\theta - \theta_f) \quad (2)$$

where θ_f is an optimizable parameter corresponding to the angle between the long axis of the MWCNT and horizontal, A is the non-dichroic intensity, and B is the dichroic intensity. Fig. 5b plots the best fit of the data to this equation. There is good agreement between the data (points, with estimated error) and the polarization fit (solid line). The fit parameters are presented in Table 2. The good fit is consistent with the intensity variation with tilt angle sampling the same physics as XLD. The polarization ratio ($I_\perp/I_\parallel$, where $I_\perp$ and $I_\parallel$ are determined from the fit to the tilt dependent intensities) is calculated to be 13.5 for the center of tube.

Table 2
Fitting parameters of EELS data.

	Observed angle[a] (deg.)	A[b]	B[b]	θ_f[b]
Fig. 5	0	0.2 ± 0.03	2.5 ± 0.03	$-88 \pm 5^\circ$
Fig. 6	20	0.8 ± 0.01	1.2 ± 0.01	$57 \pm 5^\circ$

[a] Reference line for angle determination is horizontal (clockwise is positive).
[b] From fit of measured π^* intensity to Eq. (2).

3.3. Use of ELD from q-dependent TEM-EELS to evaluate structural quality of MWCNT

In order to explore the capability to evaluate structural quality of MWCNT using ELD measured using q-dependent TEM-EELS in the matter outlined above, an imperfect MWCNT was studied and compared to the results for the high quality MWCNT (Figs. 3–5). Fig. 6a presents a low resolution TEM image of this tube, which is fairly straight and in a plane perpendicular to the beam except at ~150 nm from the tip where it bends and points upward making an angle of 67° relative to horizontal (this bend is not obvious in the TEM image). The HRTEM image (Fig. 6b) shows a lot of surface irregularities which is indicative of a damaged structure. The region enclosed in the boxes in Fig. 6a and b indicates the area studied using the q-dependent spectrum imaging technique.

C 1s spectrum images (full spectrum at each point in the image) were recorded at five tilt angles. The background subtracted, continuum normalized spectra integrated over the center region of the MWCNT are plotted in Fig. 6c. The intensity variations at the π^*-resonance as a function of tilt angle follow a trend similar to that observed for the perfect MWCNT (Fig. 5) but the extent of variation of the π^* intensity is smaller. The stronger transition at zero tilt could be due to the fact that the region is not perfectly horizontal as well as due to the defects in the tube. As the tilt angle increases the intensity of the π^*-resonance systematically increases and reaches a maximum at the highest angle measured (50°). Fig. 6d plots π^*-intensity values (black circles) as a function of tilt angle of the defective MWCNT. The polarization function gives a good fit to these experimental values indicating that, despite the presence of defects, the tube is still anisotropic with mainly sp^2 configuration. The minimum intensity is observed at -30° which corresponds to the angle between the MWCNT and the plane perpendicular to the electron beam. The polarization ratio ($I_\perp/I_\parallel$) determined from the fit to the tilt dependent intensities for the center of the tube was 2.2. This is significantly smaller than the polarization ratio for the center of the perfect MWCNT (13.5). Since the experimental conditions were similar for both measurements and the spectra were corrected for thickness variation by normalizing to the C 1s continuum jump, the difference in the measured polarization ratio reflects the relative structural quality of the tubes.

The π^* images (difference of images at 285 eV and 280 eV) at different tilt angles were assembled into a single file and then the electron linear dichroic (ELD) response at each pixel in the resulting polarization-dependent π^* tilt-stack was fit to the polarization function (Eq. (2)). Maps of the amplitude (ELD magnitude) and constant (non-dichroic component) terms were then constructed from the A and C terms of the pixel-by-pixel fit. The white rectangle superimposed on the HRTEM image (Fig. 7a) shows the region for which the amplitude (Fig. 7b) and constant (Fig. 7c) maps were obtained. The ELD map (Fig. 7b) shows the magnitude of the polarization effect at each pixel on the MWCNT. Brighter pixels correspond to stronger polarization (fewer sp^2 defects) while darker pixels correspond to weaker polarization (more sp^2 defects). The ELD amplitude map (Fig. 7b) corresponds

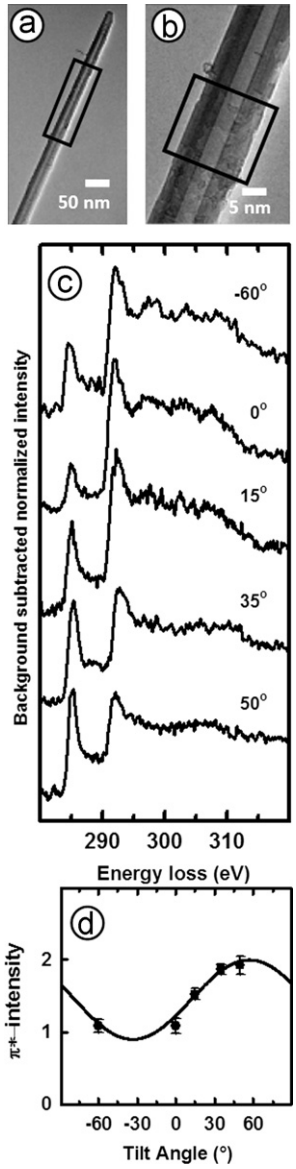

Fig. 6. (a) Low resolution and (b) high resolution TEM images of a defective MWCNT selected for angle dependent TEM-EELS studies for comparison. (c) C 1s EELS spectra of the centre of the MWCNT extracted from linescans recorded at the indicated sample tilt angles. The linescans were recorded with $q_{\perp}$ parallel to the long axis of the MWCNT. (d) π^*-intensities at the centre of the defective MWCNT (circles, with error bars) plotted versus tilt angle, fit to the polarization function (solid line). The vertical scale of (d) is the same as that for Fig. 5b.

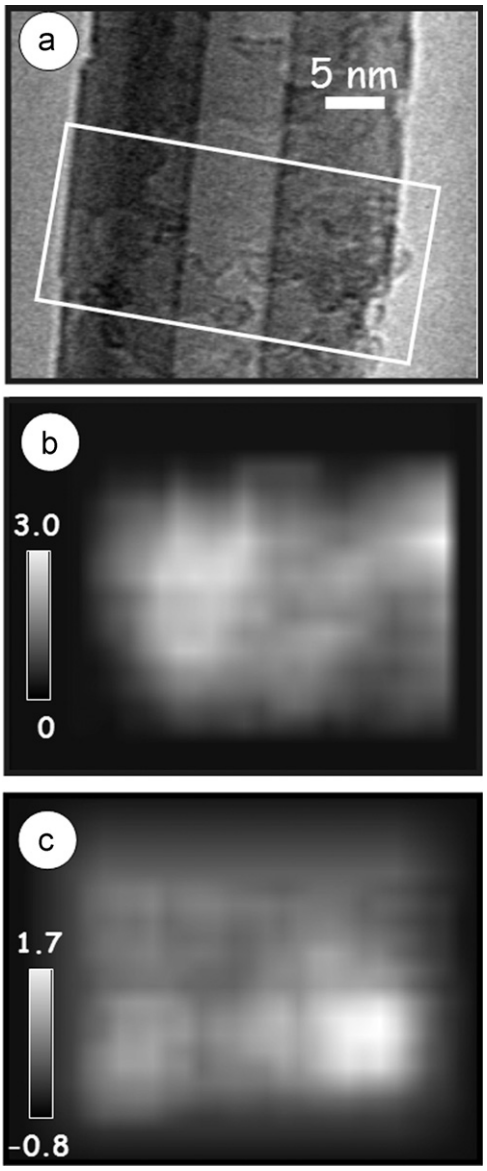

Fig. 7. (a) TEM image of the region for which q-dependent EELS was studied to measure electron linear dichroism (ELD) signals. (b) the amplitude and (c) and constant maps, obtained by fitting each pixel in the π^* polarization stack (23×18 pixels, 3 tilt angles) to Eq. (2). The amplitude and constant maps have been smoothed to reduce 'pixelation'.

relatively well to that expected from the TEM image. For instance, the region with more surface irregularities in the lower right appears darker in the ELD amplitude image. The constant map (Fig. 7c), which corresponds to the portion of the signal without ELD, is the complement to the amplitude image, with brightest pixels in the lower right region where the MWCNT is more defective. The present results clearly serve as a proof-of-principle demonstration, but are limited both by the relatively few pixels used (23×18) and the small numbers of tilt angles (3). The quality of the ELD amplitude and constant images can be significantly improved by recording data with finer pixels and at more tilt angles. While the presence of defects can be seen directly in the HRTEM image (Fig. 7a), the changes in the ELD signal provide a spectroscopic probe of the level of bonding deviation from perfect sp^2 hybridization.

4. Discussion

The conventional approach to q-dependent EELS in the TEM [21–23], where the scattering vector q is controlled by changing the magnitude of the EELS collection angle, does not provide the same dichroic effect as that observed by STXM of MWCNT [17–19]. In the conventional approach, the spatial orientation of q is not well enough defined to extract dichroic signals at the edge and center of MWCNT at various tilt angles, where a large dichroism should be observed in the C $1s \rightarrow \pi^*$ transition (Fig. A-3). In this work a large electron linear dichroism is observed in the C $1s \rightarrow \pi^*$ transition by displacing the convergent beam diffraction pattern relative to the EELS entrance aperture. The spectra recorded at different tilt angles showed an ELD signal similar to the XLD signal routinely obtained by STXM. This method effectively selects orientations of $q_{\perp}$ relative to the MWCNT while removing $q_{\parallel}$. This well-resolved directionality of q is clearly demonstrated in Fig. 4.

The large change in the intensity of the C 1s→π^* transition (Fig. 4b) shows that $q_\perp$ has been minimized and the collection of $q_\parallel$ has been limited to certain orientations with respect to the MWCT axis. This can be further improved by using a smaller entrance aperture and increasing the displacement of the distribution of the inelastic scattering signal. However, this reduces the number of electrons that enter the spectrometer and thus lowers the signal-to-noise ratio. In order to improve the quality of the spectra, one has to use a longer exposure which may cause several problems such as sample contamination, drift, and damage to the sample. The intensity of the C 1s→π^* in a high quality MWCNT could be useful to evaluate the degree to which q has been resolved as the size and location of the aperture changes.

The approach to measuring ELD documented in this work can be used to perform TEM-EELS dichroic evaluations of anisotropic samples such as carbon nanotubes that, at present, can only be done on a very small number of synchrotron spectromicroscopy beamlines, and with much lower spatial resolution than TEM-EELS provides. In principle, this method is not limited to MWCNT systems. It can also be used to characterize the ELD and thus the structural anisotropy in a variety of anisotropic systems such as $NaTiO_2$ nanorods or nanoscrolls [34], BN nano-wires and nano-fibers [35], etc. We note that high resolution transmission electron microscopy can, in favorable circumstances, visualize individual defects. However, given the experimental challenges of establishing those conditions, it is impractical to perform such measurements over a large number of defect sites. In contrast this spectroscopic method provides a means to evaluate defect distributions and structural quality over clusters or ensembles of nanostructures. Thus we consider direct high resolution imaging and this method as complementary techniques to characterize defects which affect electronic structure.

Acknowledgments

This research was supported by NSERC (Discovery Grants to APH and GAB), CFI, and the Canada Research Chair program. The Canadian Centre for Electron Microscopy (CCEM) is a Canadian national facility supported by NSERC and McMaster University.

Appendix A. Supplementary material

Supplementary data associated with this article can be found in the online version at doi:10.1016/j.ultramic.2011.11.017.

References

[1] I. Musa, M. Baxendale, G.A. Amaratunga, W. Eccleston, Synthetic Metals 102 (1999) 1250.
[2] W. Bauhofer, J. Kovaces, Composite Science and Technology 69 (2009) 1489.
[3] E. Najafi, J. Kim, S.H. Han, K. Shin, Colloids and Surfaces 257 (2005) 333.
[4] X.B. Xu, Zh.-M. Li, L. Shi, X. Bian, Zh.D. Xiang, Small 3 (2007) 408.
[5] C. Kuan, W. Chen, Y. Li, C. Chen, H. Kuan, C. Chiang, Journal of Physics and Chemistry of Solids 71 (2010) 539.
[6] V. Georgakilas, K. Kordatos, M. Prato, D.M. Guldi, M. Holzinger, A.M. Hirsch, Journal of American Chemical Society 124 (2002) 760.
[7] Y.P. Sun, K. Fu, Y. Lin, W. Huang, Accounts of Chemical Research 35 (2002) 1096.
[8] A.A. Mamedov, N.A. Kotov, N. Prato, D.M. Guldi, J.P. Wicksted, A. Hirsch, Nature Materials 1 (2002) 190.
[9] H. Kong, Ch. Gao, D. Yan, Journal of American Chemical Society 126 (2004) 412.
[10] J.P. Salvetat, A.J. Kulik, J.M. Bonard, G. Andrew, D. Briggs, T. Stöckli, K. Méténier, S. Bonnamy, F. Béguin, N.A. Burnham, L. Forró, Advanced Materials 11 (1999) 161.
[11] G. Yamamoto, J. Won Suk, J. An, R.D. Piner, T. Hashida, T. Takagi, R.S. Ruoff, Diamond and Related Materials 19 (2010) 748.
[12] J. Hone, M. Whitney, C. Piskoti, A. Zettl, Physical Review B 59 (1999) R2514.
[13] J. Charlier, Accounts of Chemical Research 35 (2002) 1063.
[14] H. Murphy, P. Papakonstantinou, T.I.T. Okpalugo, Journal of Vacuum Science and Technology B 24 (2006) 715.
[15] S. Osswald, M. Havel, Y. Gogotsi, Journal of Raman Spectroscopy 38 (2007) 728.
[16] S. Banerjee, T. Hemraj-Benny, S. Sambasivan, D.A. Fischer, J.A. Misewich, S.S. Wong, Journal of Physical Chemistry B 109 (2005) 8489.
[17] E. Najafi, D. Hernández Cruz, M. Obst, A.P. Hitchcock, B. Douhard, J.-J. Pireaux, A. Felten, Small 4 (2008) 2279.
[18] A. Felten, X. Gillon, M. Gulas, J.-J. Pireaux, X. Ke, G. Van Tendeloo, C. Bittencourt, E. Najafi, A.P. Hitchcock, ACS Nano 4 (2010) 4431.
[19] E. Najafi, J. Wang, A.P. Hitchcock, J. Guan, S. Denommee, B. Simard, Journal of American Chemical Society 132 (2010) 9020.
[20] W.L. Chao, P. Fischer, T. Tyliszczak, S. Rekawa, E. Anderson, P. Naulleau, Physical Review Letters, submitted for publication.
[21] O. Stéphan, M. Kociak, L. Henrard, K. Suenaga, A. Gloter, M. Tencé, E. Sandré, C.J. Colliex, Journal of Electron Spectroscopy and Related Phenomena 114–116 (2001) 209–217.
[22] Y. Sun, J. Yuan, Physical Review B 71 (2005) 125109.
[23] X. Hu, Y. Sun, J. Yuan, Ultramicroscopy 108 (2008) 465.
[24] G.A. Botton, C.D. Boothroyd, W.M. Stobbs, Ultramicroscopy 59 (1995) 93.
[25] G.A. Botton, Journal of Electron Spectroscopy and Related Phenomena 143 (2005) 129.
[26] K. Saitoh, K. Nagasaka, N. Tanaka, Journal of Electron Microscopy 55 (2007) 281.
[27] C. Heiliger, F. Heyroth, F. Syrowatka, H.S. Leipner, I. Maznichenko, K. Kokko, W. Hergert, I. Mertig, Physical Review B 73 (2006) 045129.
[28] K.R. Moonoosawmy, P. Kruse, Journal of American Chemical Society 130 (2008) 13417.
[29] R.F. Egerton, Electron Energy-Loss Spectroscopy in the Electron Microscope, Plenum Press, New York, 2011.
[30] R.D. Leapman, P.L. Fejes, J. Silcox, Physical Review B 28 (1983) 2361.
[31] N.D. Browning, J. Yuan, L.M. Brown, Ultramicroscopy 38 (1991) 291.
[32] G. Radtke, S. Lazar, G. Botton, Physical Review B 74 (2006) 155117.
[33] N. Yao, V. Lordi, S.X. Ma, E. Dujardin, A. Krishnan, M.M.J. Treacy, T.W. Ebbesen, Journal of MaterialsResearch 13 (1998) 2432.
[34] C.W. Peng, M. Richard-Plouet, T.-Y. Ke, C.-Y. Lee, H.-T. Chiu, C. Marhic, E. Puzenat, F. Lemoigno, L. Brohan, Chemistry of Materials 20 (2008) 7228.
[35] D. Pacil, M. Papagno, T. Skala, V. Matolin, T. Sainsbury, T. Ikuno, D. Okawa, A. Zettl, K.C. Prince, Journal of Physics: Condensed Matter 22 (2010) 295301.